Biophysical Journal
Article

Biophysical Society

The dependence of EGFR oligomerization on environment and structure: A camera-based N&B study

Harikrushnan Balasubramanian,[1] Jagadish Sankaran,[1] Shambhavi Pandey,[1] Corinna Jie Hui Goh,[1] and Thorsten Wohland[1,2,*]

[1]Department of Biological Sciences and NUS Centre for Bio-Imaging Sciences, National University of Singapore, Singapore, Singapore and [2]Department of Chemistry, National University of Singapore, Singapore, Singapore

ABSTRACT Number and brightness (N&B) analysis is a fluorescence spectroscopy technique to quantify oligomerization of the mobile fraction of proteins. Accurate results, however, rely on a good knowledge of nonfluorescent states of the fluorescent labels, especially of fluorescent proteins, which are widely used in biology. Fluorescent proteins have been characterized for confocal, but not camera-based, N&B, which allows, in principle, faster measurements over larger areas. Here, we calibrate camera-based N&B implemented on a total internal reflection fluorescence microscope for various fluorescent proteins by determining their propensity to be fluorescent. We then apply camera-based N&B in live CHO-K1 cells to determine the oligomerization state of the epidermal growth factor receptor (EGFR), a transmembrane receptor tyrosine kinase that is a crucial regulator of cell proliferation and survival with implications in many cancers. EGFR oligomerization in resting cells and its regulation by the plasma membrane microenvironment are still under debate. Therefore, we investigate the effects of extrinsic factors, including membrane organization, cytoskeletal structure, and ligand stimulation, and intrinsic factors, including mutations in various EGFR domains, on the receptor's oligomerization. Our results demonstrate that EGFR oligomerization increases with removal of cholesterol or sphingolipids or the disruption of GM3-EGFR interactions, indicating raft association. However, oligomerization is not significantly influenced by the cytoskeleton. Mutations in either I706/V948 residues or E685/E687/E690 residues in the kinase and juxtamembrane domains, respectively, lead to a decrease in oligomerization, indicating their necessity for EGFR dimerization. Finally, EGFR phosphorylation is oligomerization dependent, involving the extracellular domain (550–580 residues). Coupled with biochemical investigations, camera-based N&B indicates that EGFR oligomerization and phosphorylation are the outcomes of several molecular interactions involving the lipid content and structure of the cell membrane and multiple residues in the kinase, juxtamembrane, and extracellular domains.

SIGNIFICANCE Number and brightness (N&B) analysis is a powerful tool to determine protein association but is mostly conducted in confocal microscopes. This work determines the brightness and fluorescence probability of a range of fluorescent proteins for camera-based N&B on a total internal reflection microscope, demonstrating that with proper calibration, different fluorescent proteins provide the same answers on oligomerization within the margins of error. This camera-based approach allows measuring N&B values across whole-cell basal membranes up to an area of $\sim$1,000 μm^2 simultaneously. N&B is then used in combination with biochemical assays to investigate the oligomerization and activation of the epidermal growth factor receptor (EGFR), a prototypical receptor tyrosine kinase with importance in cell signaling, division, and survival and that is implicated in various cancers. The results indicate that EGFR oligomerization and activation are governed by an interplay between membrane structure and composition and key amino acid residues of EGFR that span the extracellular to the intracellular domains.

Submitted May 6, 2022, and accepted for publication November 1, 2022.

*Correspondence: twohland@nus.edu.sg

Harikrushnan Balasubramanian's present address is Janelia Research Campus, Howard Hughes Medical Institute, Ashburn, Virginia.

Jagadish Sankaran's present address is Genome Institute of Singapore, A*STAR, Singapore, Singapore.

Corinna Jie Hui Goh's present address is Bioinformatics Institute, A*STAR, Singapore, Singapore.

Editor: Gerhard Schutz.

https://doi.org/10.1016/j.bpj.2022.11.003

© 2022 Biophysical Society.

This is an open access article under the CC BY-NC-ND license (http://creativecommons.org/licenses/by-nc-nd/4.0/).

INTRODUCTION

Protein oligomerization or clustering is an essential process in many cell signaling pathways, and its determination and quantification in living cells is an important task in microscopy. More often than not, biological systems contain not a single species but a mixture of various oligomeric species that contribute differently to the signaling process, and their separation is difficult. Multiple techniques based on fluorescence spectroscopy (1) including Förster resonance energy transfer (FRET) (2,3), fluorescence cross correlation spectroscopy (FCCS) (4), photon counting histogram (PCH) (5), fluorescence intensity distribution analysis (FIDA) (6), spatial intensity distribution analysis (SpIDA) (7,8), image correlation spectroscopy (ICS) (9), and single-molecule photobleaching (SMP) (10) have been developed to address this challenge, with each having its own set of requirements, advantages, and disadvantages.

One of the techniques to quantify oligomerization is number and brightness (N&B) analysis (11,12), a fluorescence fluctuation spectroscopy method based on moment analysis (13,14). In this technique, the average N&B of particles is calculated from the mean and variance, i.e., the first and second moments, respectively, of the intensity fluctuations. N&B was originally established for confocal microscopy (11,12) and later expanded to camera-based total internal reflection microscopy (TIRFM) (15). Due to its computational simplicity, it is widely used for oligomerization studies of various biological molecules, including cell membrane receptors (16).

N&B is typically performed on proteins of interest fused with fluorescent proteins (FPs). The oligomerization state of a protein is determined by computing the ratio of the brightness of the protein of interest to the brightness of the monomeric state of the FP. However, not all molecules of FPs are fluorescent due to incomplete maturation, misfolding, or photobleaching (17–21). Therefore, N&B is calibrated with singly and doubly labeled biomolecules. The singly labeled sample provides a direct measure of the molecular brightness of the label. In principle, the doubly labeled sample should have twice the brightness. Deviation from this yields the probability of the label to be fluorescent. Here, we first determine the brightness and fluorescence probability of cell-membrane-bound FPs from the fluorescent protein toolbox (22) and apply it to the investigation of the oligomerization of the epidermal growth factor receptor (EGFR).

EGFR is a receptor tyrosine kinase that transduces signals through phosphorylation of intracellular tyrosine residues (23). Although EGFR has been one of the most-widely studied proteins, its resting-state conformation remains a matter of debate. The traditional view is that EGFR exists as monomers on the cell membrane prior to ligand binding and undergoes dimerization upon EGF binding. However, preformed EGFR dimers in the absence of EGF have been reported in numerous studies (Fig. S1) (6,24–37). But the dimerization levels vary greatly between studies (Table S1), and it is unclear what are the determining factors for receptor di- or oligomerization (33,38–40). Furthermore, there is evidence that full receptor activation requires higher oligomers (35,41–46). Here, we use camera-based N&B on TIRFM to determine the oligomerization of EGFR in live CHO-K1 cells and investigate the effects of the actin cytoskeleton, the plasma membrane organization, and the roles of different EGFR residues on oligomerization.

THEORY

N&B

The N&B equations for apparent number and apparent brightness using an electron-multiplying charge-coupled device (EMCCD) are (15).

$$N = \frac{(\langle I \rangle - offset)^2}{\sigma^2 - \sigma_0^2} \tag{1}$$

and

$$B = \frac{\sigma^2 - \sigma_0^2}{\langle I \rangle - offset}, \tag{2}$$

where N is the apparent number of particles in the observation volume, B is the apparent brightness of a particle, I is the average signal intensity, *offset* is the intensity offset of the camera, σ^2 is the variance of the signal, and σ_0^2 is the variance of the readout noise in the camera.

The variance of the signal is strongly influenced by shot noise of the detector, which affects the N&B values if not corrected for. Since shot noise is not correlated in time, we estimate the shot-noise-corrected variance from the covariance between consecutive frames, an approach called G1 analysis (Section S1.1; Eq. S1) (15). This is analogous to the estimation of the amplitude of the autocorrelation function, G(0), in fluorescence correlation spectroscopy (FCS), from neighboring values.

Workflow of N&B

The schematic in Fig. 1 shows the workflow of the TIRF-implemented camera-based N&B used in this study. It illustrates with an example the power of N&B to identify the proportional contribution of the N and B values to the pixel intensity from its mean and variance alone (Eqs. 1 and 2).

The *offset* and σ_0^2 are obtained from a dark image captured by the camera. The dark image also serves as a reference image to perform pixel-wise correction of fixed-pattern noise of camera images (Section S1.2).

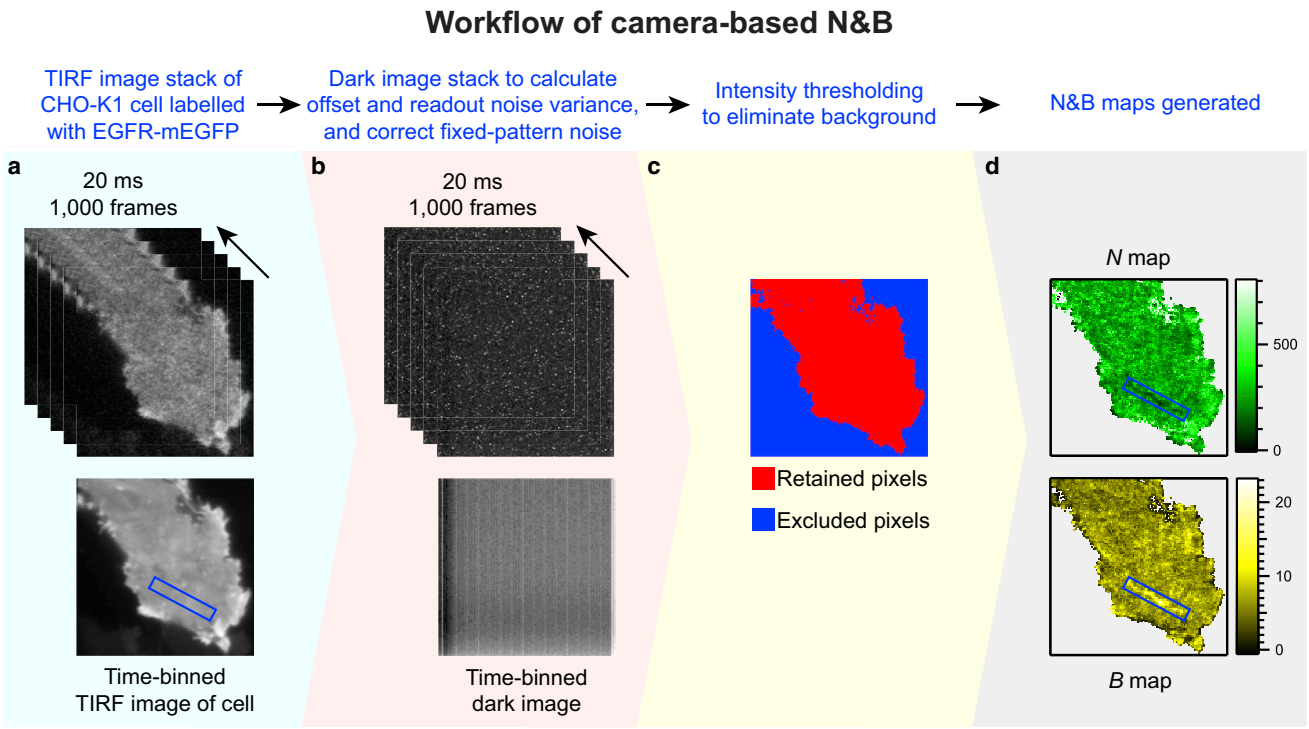

FIGURE 1 N&B workflow. (*a*) A CHO-K1 cell labeled with EGFR-mEGFP is shown as an example. The TIRF image stack of this cell contains 1,000 frames collected at 20-ms exposure time. The TIRF image after time binning of all the frames is shown at the bottom left. (*b*) A dark image stack from the camera with the same spatiotemporal characteristics as the cell image stack is used to obtain the offset and readout noise variance and to correct for fixed-pattern noise, as shown by the projection of all frames in the bottom image. (*c*) An intensity threshold (refer to data analysis in the materials and methods) is applied to exclude the background pixels (*blue*) and retain only pixels from the cell (*red*). (*d*) Applying Eqs. 1 and 2, N and B maps are generated. Although the blue box in the time-binned TIRF image shows an area whose intensity is indistinguishable from the surrounding areas, the N and B maps of the same area show that the number of particles is low and the molecular brightness is high, respectively, illustrating the utility of N&B.

Pooled brightness of cells

For a population of cells, the pooled weighted arithmetic mean brightness is calculated from the brightness values of pixels in cell images (34). Each image stack contains only one cell.

$$B_{pooled} = \frac{\sum_{j=1}^{N_c}\sum_{i=1}^{n_j}\alpha_{ij}B_{ij}}{\sum_{j=1}^{N_c}\sum_{i=1}^{n_j}\alpha_{ij}}; \quad \alpha_{i,j}\begin{cases} 0, \ if \ I_{ij} < I_{threshold} \\ 1, \ if \ I_{ij} \geq I_{threshold} \end{cases}, \tag{3}$$

where B_{pooled} is the pooled mean brightness for a population of N_c cells, n_j is the number of pixels in image j, and B_{ij} is the brightness of each pixel i in image j. α_{ij} is 1 if the intensity of a pixel (I_{ij}) is more than the intensity threshold value ($I_{threshold}$) and corresponds to pixels inside a cell, and vice versa. The error in B_{pooled} is calculated according to Eq. S3. In the rest of the article, all brightness values are pooled values.

Brightness calibration

The theory of N&B for oligomers has been published in detail in a previous publication (34). Here and in the supporting material, we provide a brief summary. The fluorescence probability p of a fluorescent protein is estimated from the ratio of the pooled apparent brightness of the dimeric FP control (B_d) to the pooled apparent brightness of the monomeric FP control (B_m) (34).

$$p = \frac{B_{\mathrm{d}}}{B_{\mathrm{m}}} - 1 \tag{4}$$

The error in p is calculated according to Eq. S4.

EGFR oligomerization calculations

In the case of EGFR experiments, we first calculate the ratio of the apparent brightness of EGFR (B_{E}) to the apparent brightness of the monomer (B_{m}).

$$r_{\mathrm{E}} = \frac{B_{\mathrm{E}}}{B_{\mathrm{m}}} \tag{5}$$

We utilize the minimum-order oligomer model (MOM) to determine whether EGFR is monomeric or whether oligomers are necessary to explain the data (34). The MOM model assumes the presence of only two species—monomers and the minimum-order oligomer species required to

explain the data. This leaves open the question of whether a mixture of more and higher oligomer species is present, but it provides a lower limit of oligomerization state and an upper limit of the fraction of monomers bound in oligomers. Using MOM, the fraction of EGFR molecules present as oligomers (e_{oligo}, refer to Fig. S3) is expressed as (34)

$$e_{oligo} = \frac{r_E - 1}{(n_{mom} - 1)p}, \quad (6)$$

where n_{mom} is the order of the minimum oligomer species. In order to determine n_{mom}, we estimate the brightness of pure higher-order oligomer samples (B_n) based on the experimental B and p values of the monomer and dimer FP controls (Fig. S4) (34).

$$B_n = B_m[(n - 1)p + 1], \quad (7)$$

where n is the oligomer species order. The errors in r_E, e_{oligo}, and B_n are calculated according to Eqs. S5, S6, and S7, respectively.

The minimum value of n yielding $B_n > B_E$ is used as n_{mom}, where $\lceil\ \rceil$ is the ceiling function.

$$n_{mom} = \left\lceil \frac{\left(\frac{B_E}{B_m} - 1\right)}{p} + 1 \right\rceil \quad (8)$$

Once the minimum order is determined, the proportion of the monomers and the minimum-order oligomers is determined using Eq. 6 (34).

It must be noted that, as with any fluctuation-based analysis, N&B analysis only detects EGFR clusters that are mobile on the measurement timescale, and any immobile clusters present would not be detected. In our previous work (34), using MOM, we observed clustering ranging from orders 2–8, while the average diffusion coefficient from imaging FCS ranged from 0.03 to 0.3 $\mu m^2/s$. Therefore, clusters of at least up to order 8 are mobile and detectable by N&B. Clusters much larger than this may be immobile and invisible to N&B. However, the MOM only reports the minimum oligomer order required to explain the data and does not comment on the upper limit of cluster size. Therefore, while MOM may not represent the true distribution of various oligomer species since it cannot resolve them in the sample, it provides apparent oligomer percentages of the mobile EGFR molecules with the understanding that they represent a minimal model of monomers and the smallest oligomer species that are consistent with the experimental data. It is therefore a useful empirical parameter to report protein oligomerization.

We define two terms, oligomerization and clustering, as follows. Oligomerization involves specific receptor-receptor interactions to form larger oligomeric units, which activate the receptor. Oligomers are typically below the diffraction limit and cannot be optically resolved. Even in areas of homogenous intensity in images, certain pixels of B values larger than the dimer calibration control are present, which are indicative of oligomers. Clustering may involve oligomerization of EGFR, grouping of receptors localized in lipid domains, or nonspecific aggregation of receptors or, most likely, a combination of all three. Clusters are seen as large and clearly defined visible patches of multiple pixels in images (e.g., refer to the *blue box* in Fig. 1).

MATERIALS AND METHODS

Sample preparation

Details of plasmids, preparation of live cell samples, drug perturbations, and Western blotting are provided in the supporting material. Full protocols for live-cell sample preparation and data acquisition and analysis are also available on Protocol Exchange (47,48).

Instrumentation

The TIRF microscopy setup included an inverted epifluorescence microscope (IX83, Olympus, Tokyo, Japan) equipped with a motorized TIRF illumination combiner (cellTIRF-4Line IX3-MITICO, Olympus). 405- (LAS/405/100/D, Olympus), 488- (LAS/488/100, Olympus), and 561-nm lasers (LAS/561/100, Olympus) were connected to the TIRF illumination combiner. The 488-nm laser was equipped with a clean-up filter (FF01-488/6-25, Semrock, Rochester, NY, USA). A 100× numerical aperture 1.49 oil-immersion objective (Apo N, Olympus) was used. The immersion oil used had a refractive index of 1.518 (IMMOIL-F30CC, Olympus). A quad band dichroic (ZT405/488/561/640rpc, Chroma Technology, Bellows Falls, Vermont, USA) was used to direct the laser to the sample and allow the fluorescence emission to pass through. The fluorescence emission was passed through a quad band emission filter (ZET405/488/561/640m, Chroma Technology). An EMCCD (iXon^{EM}+ 860, 24-μm pixel size, 128 × 128 pixels, Andor, Oxford Instruments, Oxfordshire, UK) camera was used for detection. For the cell measurements, 37°C temperature and 5% CO_2 atmosphere were maintained using an on-stage incubator (Chamlide TC, Live Cell Instrument, Seoul, South Korea).

Data acquisition

We used 100 μW power (as measured in the back focal plane of the objective) for all lasers. The penetration depth was set at 100 nm. The software Andor Solis (v.4.31.30037.0-64-bit) was used for image acquisition. The following camera settings were used for the EMCCD: mode of image acquisition = kinetic; baseline clamp (i.e., offset) = "on" to minimize the baseline fluctuation; pixel readout speed = 10 MHz; maximum analog-to-digital gain = 4.7; vertical shift speed = 0.45 μs; and electron multiplying gain = 300. The EMCCD was operated after cooling to −80°C. A stack of 1,000 frames (128 × 128 pixels) were collected at 50 frames per second. The recorded image stacks were saved as 16-bit tiff files. A dark image was collected with the camera shutter closed using the same acquisition parameters.

Data analysis

The data analyses were performed on a computer equipped with a GPU with the following configuration: Windows 10 Home 64-bit operating system, Intel Core i7-7800× CPU @ 3.50-GHz processor, 32-GB RAM, and

NVIDIA TITAN Xp GPU with 3,840 CUDA cores and 12.3-GB memory. The image stacks were loaded into the GPU-driven ImFCS 1.52 plugin (34,49) in Fiji. A polynomial of order two was used to correct for photobleaching. Intensity thresholding was performed to include only pixels within the cell. Background correction was performed using a dark image with the same spatiotemporal dimensions as the measurement image.

RESULTS AND DISCUSSION

Brightness calibration for N&B

Optimization of acquisition parameters for N&B

Camera-based N&B using G1 analysis requires an exposure time that is shorter than the time a particle needs to diffuse through the observation area of a pixel but long enough to obtain a stable N&B signal with a high signal-to-noise ratio (34,50). This time was determined to be 20 ms for our camera-based system (34). Moreover, an exposure time of 20 ms allowed effective intensity thresholding of the pixels to separate the cell from the background.

The PMT-mEGFP$_2$/PMT-mEGFP brightness ratio measured at 20-ms exposure time was determined for total acquisition times from 1 to 100 s. It is variable below 10 s and then stabilized at ~1.8 (Fig. S5). In this work, we used 20 s for all measurements as a compromise between acquisition speed and accuracy and precision. Measurements had photobleaching, i.e., a steady decay of intensity, that influences the variance and thus the calculated N and B values. Therefore, a photobleaching correction, using a polynomial of second degree (51,52), is applied to avoid influence of the decaying intensity on N&B, very similar to fluorescence correlation spectroscopy (16,53,54). Example B maps and intensity traces for PMT-mEGFP, PMT-mEGFP$_2$, and EGFR-mEGFP are shown in Fig. S6 to illustrate the effect of photobleaching on B values.

Brightness calibration of various fluorescent proteins

We performed brightness calibration for seven different FPs (mTurquoise2 (62), mEGFP (63), mApple (64), mCherry (65), mCherry2 (66), mScarlet (59), and mKate2 (67)). It is critical that the FPs used are predominantly monomeric and do not have a tendency to form homo-oligomers. The monomericities as reported in literature for the various FPs tested in this study are provided in Table 1. mEGFP exhibits a fluorescence probability p of 0.81 ± 0.01, which is the highest among all the tested FPs. Among the other FPs, p varied between 30% and 65%. These p values are consistent with those reported in previous studies using confocal microscopy (17,19).

In theory, knowledge of the p value allows any FP of choice to be used for obtaining reliable oligomerization results, as we demonstrated comparing mEGFP and mApple (34). But as can be seen from Table 1, many FPs considered monomeric are not truly so. FP homo-oligomerization affects the brightness calibration and also introduces uncertainty in the oligomerization estimates of the protein under investigation. Moreover, FPs with higher p values are better for visualization of labeled samples since more molecules are fluorescent. In this study, we used mEGFP, which is highly monomeric (97%–98% (18,58)) and has high fluorescence probability ($p = 0.81 \pm 0.01$).

EGFR oligomerization in resting state determined by N&B

In resting cells, the mean brightness (B_E) of EGFR-mEGFP is 3.39 ± 0.02 (Table 2). The B values of the calibration controls PMT-mEGFP and PMT-mEGFP$_2$ are 2.32 ± 0.01 and 4.21 ± 0.02, respectively (Table 1). Since 81% of mEGFP molecules are fluorescent, r_E (refer to Eq. 5) <1.81 can be explained by a dimerization model, while a higher oligomerization model is required to explain $r_E > 1.81$. Here, $r_E = 1.46$ is explained using a dimerization model. This r_E value suggests the dimerization of 57% ± 2% of EGFR molecules in resting cells. This is in agreement with 50%–70% dimerization reported in the resting state for the same cell line in previous studies (6,32,33,35,68). The ~60% dimerization observed is similar to what we had

TABLE 1 Brightness calibration of various fluorescent proteins

Fluorescent protein	Monomericity reported in literature, %	Brightness calibration control	Cells	B[a]	p[a]
mTurquoise2	88–94 (18,55)	PMT-mTurquoise2	17	1.83 ± 0.02	0.39 ± 0.02
		PMT-mTurquoise2$_2$	18	2.54 ± 0.02	
mEGFP	97–98 (18,56–58)	PMT-mEGFP	21	2.32 ± 0.01	0.81 ± 0.01
		PMT-mEGFP$_2$	18	4.21 ± 0.02	
mApple	87–95 (18,59)	PMT-mApple	20	1.38 ± 0.03	0.53 ± 0.03
		PMT-mApple$_2$	21	2.11 ± 0.02	
mScarlet	80 (59)	PMT-mScarlet	19	3.74 ± 0.03	0.54 ± 0.03
		PMT-mScarlet$_2$	15	5.75 ± 0.02	
mCherry	69–95 (18,59–61)	PMT-mCherry	16	0.86 ± 0.04	0.32 ± 0.03
		PMT-mCherry$_2$	18	1.14 ± 0.04	
mCherry2	not reported in literature yet	PMT-mCherry2	15	0.83 ± 0.04	0.64 ± 0.03
		PMT-mCherry2$_2$	16	1.36 ± 0.04	
mKate2	59–81 (18,59)	PMT-mKate2	17	1.17 ± 0.04	0.52 ± 0.04
		PMT-mKate2$_2$	18	1.78 ± 0.04	

The number of pixels in each cell is different due to differential intensity filtering in each case, but each cell had at least 3,000 and at most 17,000 valid pixels.
[a]The reported values for B and p are in terms of mean ± SE.

TABLE 2 N&B of EGFR-mEGFP in resting state, after ligand stimulation, and when subjected to various drug treatments

Plasmid construct	Treatment	Cells	B_E[a]	r_E[a]	Minimum oligomer order	Fraction of EGFR molecules in oligomers (e_{oligo})[a]
EGFR-mEGFP	Resting	24	3.39 ± 0.02	1.46 ± 0.01	2	0.57 ± 0.02
	10 ng/mL EGF	11	3.96 ± 0.06	1.71 ± 0.03	2	0.87 ± 0.04
	100 ng/mL EGF	10	5.26 ± 0.05	2.26 ± 0.03	3	0.78 ± 0.02
	3 μM LAT-A	10	3.45 ± 0.03	1.49 ± 0.02	2	0.60 ± 0.02
	2 μM Myriocin	10	3.70 ± 0.02	1.78 ± 0.02	2	0.73 ± 0.02
	3mM MβCD	10	4.13 ± 0.04	1.59 ± 0.01	2	0.96 ± 0.03
	3 μM LAT-A + 100 ng/mL EGF	7	5.72 ± 0.30	2.46 ± 0.13	3	0.90 ± 0.08
	3 mM MβCD +100 ng/mL EGF	5	6.64 ± 0.16	2.86 ± 0.07	4	0.76 ± 0.03

The e_{oligo} calculations uses the results from the brightness calibration for mEGFP, which were pmEGFP = 0.81 ± 0.01; Bm (PMT-mEGFP) = 2.32 ± 0.01; and Bd (PMT-mEGFP2) = 4.21 ± 0.02. The number of pixels in each cell is different due to differential intensity filtering in each case, but each cell had at least 600 and at most 17,000 valid pixels. Parts of these data are also provided again in Tables 3 and S2.
[a]The reported values for B_E, r_E and e_{oligo} are in terms of mean ± SE.

observed in our previous publication (34) where we tagged EGFR with mApple.

The average B values of the cells expressing EGFR-mEGFP ($n = 10$; Fig. S7) do not vary with EGFR expression levels. Intensity counts of the images are a qualitative proxy for expression levels, and our measurements were on cells whose time-averaged pixel intensities ranged from 500 to 8,000 counts. In camera-based approaches, determination of numbers of receptors per pixel require calibration measurements (53). This can be achieved through the use of calibration beads with either a known number of antibody-binding sites (69) or a known number of GFP molecules (70). The EGFR expression levels in this system were previously quantified using confocal FCS, showing between 10,000 and 1.6 million receptors per cell (33,68). Measurements in this work fall within the same range. As shown previously, dimerization levels do not depend on expression levels (33), and thus we observe similar results here (Fig. S7).

EGFR oligomerization after low- and high-dose EGF stimulation

Low- and high-dose ligand stimulation of EGFR was achieved using 10 and 100 ng/mL EGF, respectively (Fig. 2). In both cases, there was an increase in B_E by 1.17- and 1.55-fold, respectively, from the resting state. The B_E values of 3.96 ± 0.06 (10 ng/mL EGF) and 5.26 ± 0.05 (100 ng/mL EGF) (Table 2) correspond to r_E values of 1.71 and 2.27, respectively. In the case of 10 ng/mL EGF stimulation, $r_E = 1.71$ is explained by a dimerization model and translates to 87% ± 4% of EGFR receptors forming dimers.

In the case of 100 ng/mL EGF stimulation, $r_E = 2.27$ cannot be explained by a dimerization model. An oligomerization model is invoked to explain the r_E value. Using MOM, the minimum-order oligomer required to explain $r_E = 2.27$ is a trimer. Hence, this r_E value translates to 78% ± 2% of EGFR molecules forming trimers. Note that this does not imply that only EGFR monomers and trimers are present or that trimers are the dominant oligomeric species. It is very likely that several oligomeric species are present (6,35,71), and some studies using homo-FRET have suggested that tetramers are the dominant oligomeric species (41–43,72).

Effects of plasma membrane components on EGFR oligomerization

EGFR oligomerization was investigated after perturbation of the cells with various drugs (refer to supporting materials and methods) that are known to affect EGFR organization and functioning. The results from all these measurements are shown in Table 2, and representative schematics and brightness histograms are shown in Fig. 2.

EGFR oligomerization after actin depolymerization using LAT-A

After treatment with 3 μM latrunculin A (LAT-A) to test the effects of actin depolymerization on EGFR clustering (Fig. 2), we measured a B_E of 3.45 ± 0.03 (Table 2). The value of r_E of 1.49 thus remained similar to the resting state with an r_E of 1.46, indicating that the cytoskeleton does not influence EGFR oligomerization. Our results are consistent with studies using FCCS and fluorescence lifetime imaging FRET (33,73).

EGFR oligomerization after cholesterol depletion using MβCD

Numerous studies have reported that a part of the EGFR population is trapped in lipid domains (6,33,74–80). Since lipid domains are enriched in cholesterol (81), cholesterol depletion disrupts these domains. We treated cells with 3 mM methyl-β-cyclodextrin (MβCD) to investigate the effect of cholesterol depletion on EGFR oligomerization (Fig. 2). After treatment, the B_E value increased to 4.13 ± 0.04 (Table 2), which is a 1.2-fold increase from the resting state. The r_E value of 1.78 indicates at least strong dimerization with 96% ± 3% of EGFR molecules dimerizing.

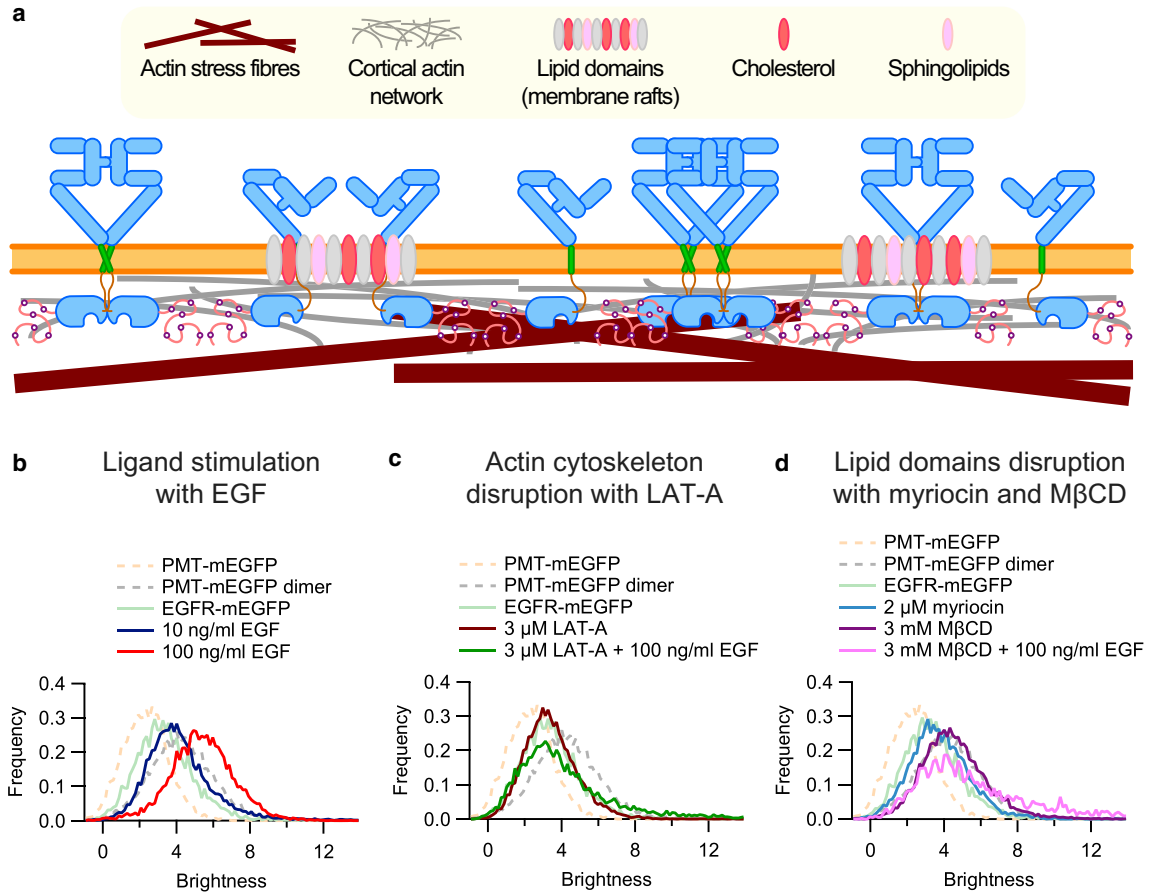

FIGURE 2 Brightness distributions of EGFR-mEGFP after ligand stimulation and drug perturbations. (*a*) This schematic shows EGFR distribution on the plasma membrane. The underlying actin cytoskeleton (stress fibers and cortical actin) provides stability to the plasma membrane. EGFR is present as monomers, dimers, and oligomers. A fraction of the EGFR population is trapped in lipid domains. Representative brightness histograms are shown here for the calibration controls (*light pink* and *gray dashed curves*), EGFR-mEGFP in resting state (*light green curve*), and the results of the drug treatments: (*b*) 10 and 100 ng/mL EGF stimulation (*blue* and *red curves*), (*c*) actin cytoskeleton disruption with 3 μM LAT-A (*brown curve*) followed by 100 ng/mL EGF stimulation (*dark green curve*), and (*d*) disruption of lipid domains with either 2 μM myriocin (*blue curve*) or 3 mM MβCD (*purple curve*), followed by 100 ng/mL EGF stimulation (for MβCD-induced cholesterol depletion only; *pink curve*).

These results suggest that EGFR oligomerization is hindered by trapping of EGFR molecules in lipid domains. Depletion of cholesterol perturbs these domains and releases the trapped EGFR molecules. The freed receptors interact with each other to form oligomers. Other studies have also reported an increase in EGFR oligomerization and phosphorylation after cholesterol depletion using both biochemical (cross-linking, immunoprecipitation) and biophysical (FCCS, SMP, immunoelectron microscopy) techniques (6,33,74–80).

EGFR oligomerization after sphingolipid depletion using myriocin

Sphingolipids are also a core component of lipid domains (81) and represent an alternative target to perturb these domains. The importance of sphingolipids in EGFR clustering was investigated using 2 μM myriocin, which interferes with sphingolipid synthesis (Fig. 2) (81,82). We measured a B_E value of 3.70 ± 0.02 (Table 2), which is a 1.09-fold increase compared with the resting state with a concomitant value of $r_E = 1.60$. These data can be explained by 73% ± 2% of EGFR molecules existing in dimers. This indicates that myriocin treatment is able to free a fraction of the receptors from the lipid domains and increases their probability to interact and oligomerize, although its effect is not as strong as that of MβCD (83).

EGFR oligomerization upon EGF stimulation following actin cytoskeleton disruption or cholesterol depletion

The effects of EGF stimulation were also tested post actin cytoskeleton disruption and cholesterol depletion (Fig. 2). While LAT-A-induced actin cytoskeleton depolymerization by itself had not shown any effect on EGFR oligomerization, it increased EGFR oligomerization following 100 ng/mL EGF stimulation. A B_E of 5.72 ± 0.30 (Table 2) was

observed, which is 1.69-, 1.66-, and 1.09-fold higher than the resting state, after LAT-A treatment or after 100 ng/mL EGF stimulation, respectively. The resulting r_E of 2.46 requires a trimerization model to explain it and translates to 90% ± 8% of EGFR receptors forming trimers.

A similar effect of seen after 100 ng/mL EGF stimulation following cholesterol depletion using MβCD. The observed B_E of 6.64 ± 0.16 (Table 2) is 1.96-, 1.61-, and 1.26-fold higher than the resting state after MβCD treatment or after 100 ng/mL EGF stimulation, respectively. The resulting r_E of 2.86 requires a tetramerization model to explain it, with 76% ± 3% of EGFR receptors present as tetramers.

An interesting observation that can be seen in Fig. 2 is that after EGF stimulation following either LAT-A or MβCD treatment, the histogram peak does not noticeably shift, but a long right tail develops (also seen as an increase in the mean ± SE of B_E in Table 2). So, while the MOM only predicts the minimum presence of trimers or tetramers from the average value over a whole cell, the histogram indicates there is heterogeneity in EGFR distribution on the cell membrane, with some areas containing large clusters of oligomer order >4. The tail of the histogram tapers off at B_E values of ∼14, and the MOM (Eq. 7 predicts the brightness of a pure octamer sample as $B_o \sim 15.5$) suggests that we observe some clusters containing at least octamers, which is in line with our previous study (34). This does not rule out the presence of higher-order oligomers that might be immobile and not detected by N&B analysis.

The formation of such large clusters after the same perturbations was also reported in a previous publication (74). This increase in clustering, higher than that achieved from EGF stimulation alone, is attributed to the fact that cholesterol depletion or actin cytoskeleton disruption impairs EGFR endocytosis, resulting in EGFR clusters remaining on the cell membrane for a prolonged period of time and possibly merging into larger clusters (74). These clusters are also possibly localized at internalization sites (34), and it would be an interesting direction of future investigation in the context of EGFR endocytosis.

The results from the different treatments indicate that EGF stimulation influences EGFR clustering more strongly compared with the actin cytoskeleton and lipid domains. In fact, the effect of ligand stimulation becomes even more pronounced after actin cytoskeleton disruption or cholesterol depletion. The EGF-induced clustering in cholesterol-depleted cells is stronger than in cytoskeleton-disrupted cells, which might arise due to the receptors being able to cluster more easily after being initially freed by the disruption of lipid domains.

Effects of EGFR residues on EGFR oligomerization

Here, we investigate the importance of various regions in EGFR molecules in EGFR clustering by creating point and deletion mutants in those regions. The mutants were tested in the resting state and after low- and high-dose EGF stimulation.

Four mutants were created: $EGFR^{I706Q/V948R}$-mEGFP (84), $EGFR^{E685A/E687A/E690A}$-mEGFP (85), $EGFR^{K642G}$-mEGFP (86), and $EGFR^{\Delta 550\text{-}580}$-mEGFP (87). The results from the N&B of these mutants are shown in Table 3, and representative brightness histograms are shown in Fig. 3. Furthermore, Western-blot-based phosphorylation assays were conducted to corroborate the N&B data from a biochemical perspective, and the results are shown in Fig. S8.

TABLE 3 N&B of EGFR-mEGFP and EGFR-mEGFP mutants in resting state and after EGF stimulation

Mutation	Treatment	Cells	B_E[a]	r_E[a]	Minimum oligomer order	Fraction of EGFR molecules in oligomers (e_{oligo})[a]	Relative phosphorylation (Fig. S8)
EGFR-mEGFP	Resting	24	3.39 ± 0.02	1.46 ± 0.01	2	0.57 ± 0.02	0
	10 ng/mL EGF	11	3.96 ± 0.06	1.71 ± 0.03	2	0.87 ± 0.04	NA
	100 ng/mL EGF	10	5.26 ± 0.05	2.26 ± 0.03	3	0.78 ± 0.02	1
I706Q/	Resting	28	2.88 ± 0.02	1.24 ± 0.01	2	0.29 ± 0.01	0.1
V948R	10 ng/mL EGF	10	3.20 ± 0.02	1.38 ± 0.01	2	0.46 ± 0.02	NA
	100 ng/mL EGF	10	3.36 ± 0.02	1.44 ± 0.01	2	0.55 ± 0.02	0.1
E685A/	Resting	28	2.69 ± 0.02	1.46 ± 0.01	2	0.19 ± 0.01	0
E687A/	10 ng/mL EGF	12	3.33 ± 0.03	1.16 ± 0.01	2	0.53 ± 0.02	NA
E690A	100 ng/mL EGF	13	4.69 ± 0.04	1.43 ± 0.02	3	0.63 ± 0.02	1.8
K642G	Resting	21	4.11 ± 0.03	1.77 ± 0.02	2	0.95 ± 0.03	0.4
	10 ng/mL EGF	13	4.73 ± 0.03	2.04 ± 0.02	3	0.64 ± 0.02	NA
	100 ng/mL EGF	12	5.53 ± 0.06	2.38 ± 0.03	3	0.85 ± 0.02	6.4
Δ550-580	Resting	21	3.18 ± 0.02	1.37 ± 0.01	2	0.45 ± 0.02	0.2
	10 ng/mL EGF	10	3.40 ± 0.03	1.47 ± 0.02	2	0.58 ± 0.01	NA
	100 ng/mL EGF	10	3.64 ± 0.02	1.57 ± 0.01	2	0.70 ± 0.02	0.1

The e_{oligo} calculations uses the results from the brightness calibration for mEGFP, which were $p_{mEGFP} = 0.81 \pm 0.01$; B_m (PMT-mEGFP) = 2.32 ± 0.01; and B_d (PMT-mEGFP$_2$) = 4.21 ± 0.02. The number of pixels in each cell is different due to differential intensity filtering in each case, but each cell had at least 500 and at most 17,000 valid pixels. The data in the first three rows are also provided in Table 2. Parts of these data in this table are also provided in Table S2.
[a]The reported values for B_E, r_E, and e_{oligo} are in terms of mean ± SE.

EGFR$^{I706Q/V948R}$-mEGFP: TKD double mutant with impaired activator and receiver function

The mutations I706Q and V948R are located on the N-terminal and C-terminal lobes, respectively, in the tyrosine kinase domain (TKD) of EGFR. These mutations disrupt the asymmetric dimer interface formed by EGFR kinase domains and cause the loss of activator and receiver functions, respectively, leading to reduced phosphorylation and activation (84,88).

The average brightness of this mutant in the resting state is $B_E^{IQ/VR} = 2.88 \pm 0.02$ (Table 3), which is a 1.2-fold reduction compared with B_E of EGFR-mEGFP in the resting state. The $r_E^{IQ/VR} = 1.24$ is explainable by the dimerization of 29% ± 1% of EGFR molecules. This is a twofold reduction compared with the 57% ± 2% dimerization seen in the non-mutated receptor. The dimerization in the resting state is not completely abolished, suggesting that other EGFR residues and/or the plasma membrane environment are also involved in the formation of preformed EGFR dimers. Our results are in agreement with earlier reports using FCCS and SMP, which showed that resting-state oligomerization was reduced compared with EGFR-mEGFP (33,87).

Upon 10 ng/mL EGF stimulation and 100 ng/mL EGF stimulation, $B_E^{IQ/VR}$ increases to 3.20 ± 0.02 and 3.36 ± 0.02 (Table 3), which are a 1.1-fold and 1.2-fold increase, respectively, from the resting state. The $r_E^{IQ/VR}$ of 1.38 and 1.44 translates to 46% ± 2% and 55% ± 2% dimerization, respectively.

The phosphorylation assay showed very low phosphorylation in the resting state (Fig. S8, *lane 9*). Unlike in the case of EGFR-mEGFP (Fig. S8, *lanes 5 and 6*), there was also no increase in phosphorylation observed after 100 ng/mL EGF stimulation (Fig. S8, *lane 10*) (84,87). The results imply that the N-terminal activator and C-terminal receiver lobes are involved in the formation of EGFR dimers in both resting and activated state.

EGFR$^{E685A/E687A/E690A}$-mEGFP: JM-A triple mutant lacking negative cooperativity in EGF binding

EGFR exhibits negative cooperativity in EGF binding (85,89–92). The presence of negative cooperativity suggests the presence of preformed dimers, as monomers cannot

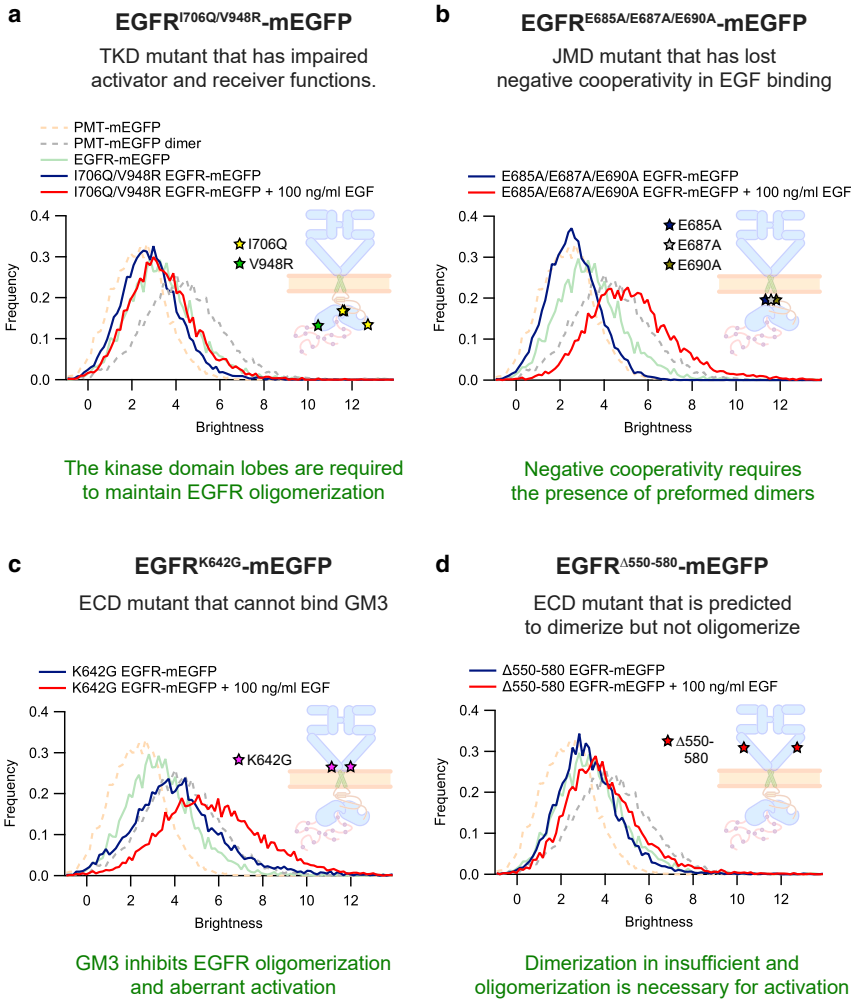

FIGURE 3 Brightness distributions of EGFR-mEGFP mutants. (*a–d*) Representative brightness histograms are shown here for the calibration controls (*cream* and *gray dashed curves*), EGFR-mEGFP in resting state (*green curve*), and EGFR mutants in resting state (*blue curve*) and after ligand stimulation (*red curve*). The 100 ng/mL EGF treatment curves for EGFR$^{E685A/E687A/E690A}$-mEGFP and EGFR^{K642G}-mEGFP have brightness values higher than the dimer calibration control that indicate the formation of higher-order oligomers.

explain cooperativity. The juxtamembrane domain (JMD) has been shown to interact with PIP_2 (26,93,94) and is also crucial in maintaining negative cooperativity. Three glutamine residues in the juxtamembrane-A (JM-A) domain are predicted to be involved in interhelical salt bridges to stabilize the helical dimer. A triple mutant (E685A/E687A/E690A) that removes these ionic interactions has been shown, using radioligand binding assays, to result in a loss of negative cooperativity in EGF binding (85). This mutant was tested by N&B to directly observe if EGFR dimerization was affected.

The average B in the resting state is $B_E^{3EA} = 2.69 \pm 0.02$, which is a 1.3-fold decrease from B_E of EGFR-mEGFP in the resting state. The $r_E^{3EA} = 1.16$ is explainable by 19% ± 1% of EGFR molecules forming dimers. This is a threefold reduction compared with the 57% ± 2% dimerization seen in the nonmutated receptor. Upon 10 ng/mL EGF stimulation, B_E^{3EA} increases to 3.33 ± 0.03 (Table 3), which is a 1.2-fold increase from the resting state. The $r_E^{3EA} = 1.43$ is explainable by a dimerization model and translates to 46% ± 2% EGFR molecules being present as dimers. Upon 100 ng/mL EGF stimulation, B_E^{3EA} increases to 4.69 ± 0.03 (Table 3), which is a 1.7-fold increase from the resting state. The $r_E^{3EA} = 2.02$ cannot be explained by a dimerization model since $r_E^{3EA} > 1.81$. The minimum-order oligomer required is a trimer with 63% ± 2% EGFR molecules being present within trimers.

The phosphorylation assay showed no phosphorylation in the resting state (Fig. S8, *lane 11*). Upon 100 ng/mL EGF stimulation, increased phosphorylation was observed (Fig. S8, *lane 12*), similar to the case of EGFR-mEGFP (Fig. S8, *lanes 5 and 6*). The results imply that the three JM-A residues are involved in the formation of preformed dimers and that mutating these residues destabilizes EGFR dimers. Thus, negative cooperativity is linked to the presence of preformed dimers, and the loss in negative cooperativity, as observed earlier by radioligand binding assays, is validated by the quantification in this study. There is ∼20% dimerization still present in the resting state, which indicates the involvement of other EGFR residues and/or plasma membrane components in maintaining EGFR preformed dimers. Furthermore, the EGFR molecules are able to oligomerize and be phosphorylated after EGF stimulation. This suggests these JM-A residues either do not interfere with the formation of activated EGFR dimers or that their effects are overcome by other interactions in the EGF-bound receptor.

$EGFR^{K642G}$-mEGFP: ECD mutant insensitive to GM3 inhibition

The ganglioside GM3 has been shown by cross-linking, Western-blot phosphorylation assays and FRET to bind to EGFR and suppress oligomerization and autophosphorylation in the absence of EGF, thereby preventing aberrant activation of the receptor (86,95–98). The GM3-EGFR interaction is mediated through a membrane proximal lysine located in the subdomain IV of the extracellular domain (ECD). Mutation of this residue to glycine (K642G) was shown to remove GM3 binding to EGFR by simulations (97) and in phase-separated liquid-disordered/liquid-ordered proteoliposomes (86). To complement these previous biochemical studies on purified systems, we tested this mutant by N&B in CHO-K1 cells (GM3 makes up 0.30% ± 0.15% of total phospholipid content in this cell line (99)) to determine whether GM3-EGFR interactions are involved in EGFR clustering in live cells.

The average B in the resting state is $B_E^{KG} = 4.11 \pm 0.03$ (Table 3), which is a 1.2-fold increase from B_E of EGFR-mEGFP in the resting state. The $r_E^{KG} = 1.77$ is explained by the dimerization of 95% ± 3% EGFR molecules. Upon stimulation using 10 ng/mL EGF and 100 ng/mL EGF, B_E^{KG} increased to 4.73 ± 0.03 and 5.53 ± 0.06 (Table 3), respectively. This represents a 1.2- and 1.4-fold increase from the resting state, with r_E^{KG} being 2.04 and 2.38, respectively. The minimum-order oligomer required to explain the data is a trimer. Using MOM, $r_E^{KG} = 2.04$ and $r_E^{KG} = 2.38$ is explained by the trimerization of 64% ± 2% and 85% ± 2% of EGFR molecules, respectively.

These results in live cells are in agreement with earlier observations in phase-separated proteoliposomes (86). The K642G mutation renders EGFR insensitive to GM3 inhibition and causes an increase in resting-state dimerization and phosphorylation. The results are also in line with the increase in dimerization observed after disruption of lipid domains, of which GM3 is presumably a component (100).

Given the variability in GM3 concentration across cell lines, it would be interesting to investigate whether there is a negative correlation between EGFR dimerization proportions and GM3 concentrations in the resting state using N&B in the future.

The phosphorylation assay showed a small increase in phosphorylation in the resting state (Fig. S8, *lane 13*) when compared with EGFR-mEGFP in the resting state (Fig. S8, *lane 5*). Stimulation with 100 ng/mL EGF resulted in high phosphorylation (Fig. S8, *lane 14*). This indicates that while release of GM3 inhibition allows EGFR to dimerize, EGF binding plays a role in forming higher-order oligomers that are necessary to properly activate the receptor. The requirement for higher-order oligomers to activate EGFR signaling has been suggested by other studies as well (35,41–43,45,46,72), and this theory is further tested by a multimerization-deficient mutant.

$EGFR^{\Delta 550\text{-}580}$-mEGFP: Multimerization-deficient ECD deletion mutant

The residues from 550 to 580 in domain IV of EGFR have been predicted by simulations to be involved in multimerization but not dimerization of EGFR. SMP measurements

in *Xenopus* oocytes revealed that several point mutations in this region resulted in reduced multimerization, reduced phosphorylation, and similar dimerization compared with wild-type EGFR (87). We created an EGFR mutant by deleting the entire region containing the residues 550 to 580 and probed it by N&B.

The average B in the resting state is $B_E^{3EA} = 3.18 \pm 0.02$ (Table 3), a 1.1-fold decrease from EGFR-mEGFP in the resting state. The $r_E^{3EA} = 1.37$ translates to 45% ± 2% of EGFR molecules forming dimers. This is a 1.3-fold reduction compared with the 57% ± 2% dimerization seen in the nonmutated receptor. Upon 10 and 100 ng/mL EGF stimulation B_E^{3EA} increases to 3.40 ± 0.03 and 3.64 ± 0.02 (Table 3), which is a 1.1- and 1.2-fold increase, respectively, from the resting state. The corresponding r_E^{3EA} of 1.47 and 1.57 can be explained by the dimerization of 58% ± 1% and 70% ± 2% of the EGFR molecules, respectively.

The phosphorylation assay showed very low levels of phosphorylation in the resting state (Fig. S8, *lane 15*). Upon 100 ng/mL EGF stimulation, no increase in phosphorylation was observed (Fig. S8, *lane 16*), unlike in the case of EGFR-mEGFP (Fig. S8, *lanes 5 and 6*).

The average dimerization of the mutant (45% ± 2%) is less than that of EGFR-mEGFP (57% ± 2%). This reduction was also seen using SMP in an earlier study, where computational modeling indicated that the formation of higher-order preformed oligomers is disrupted but dimerization is mostly unaffected (87). Moreover, the results of EGF stimulation for this mutant can be explained using an MOM model of order two, unlike the nonmutated receptor that required order three. This indicates that while some dimer formation probably occurred, higher-order oligomerization could not be induced by EGF stimulation. Furthermore, no increase in phosphorylation is observed after 100 ng/mL EGF stimulation.

Put together, the data suggest that the region containing residues 550 to 580 is involved in multimerization of EGFR and that dimer formation alone is insufficient to phosphorylate EGFR. This points toward a model where EGFR multimerization is necessary to activate the receptor through phosphorylation and initiate downstream signaling. This is consistent with other studies that have also reported that dimers are not sufficient and that higher-order oligomers like tetramers are necessary for EGFR signaling (35,41–43,45,46,72). It must be noted that we only report reduced oligomerization and phosphorylation in this study. The effect on actual receptor activation needs further experimental evidence through observation of recruited downstream proteins.

Effects of actin cytoskeleton disruption and cholesterol depletion on the mutants

We studied the effects of actin cytoskeleton depolymerization using 3 μM LAT-A, cholesterol depletion using 3 mM MβCD, and 100 ng/mL EGF stimulation following these treatments on the EGFR mutants. The results are shown in Table S2. The results for all mutants showed a similar trend in oligomerization to that seen with EGFR-mEGFP upon similar treatments. EGFR oligomerization after actin cytoskeleton depolymerization was similar to the resting state, indicating that the actin cytoskeleton did not significantly influence oligomerization (33,73). There was an increase in clustering after cholesterol depletion, indicating that the receptors cluster after being released from lipid domains (6,33,78). Interestingly, the EGFR^{K642G}-mEGFP mutant also showed an increase in clustering after cholesterol depletion despite loss of interaction with GM3, which is presumably associated with lipid domains (100). This indicates that GM3 interaction might not be solely responsible for EGFR trapping in lipid domains, and there might be other components and mechanisms that play a role.

Finally, 100 ng/mL EGF stimulation after either of these treatments increased EGFR clustering further, to levels higher than those achieved with ligand stimulation alone. Thus, the mutants confirm this effect that was initially observed with EGFR-mEGFP. This more pronounced clustering is possibly due to impairment of EGFR endocytosis by cholesterol depletion or actin cytoskeleton disruption, which causes EGFR clusters to remain on the cell membrane for a prolonged period of time and to merge into larger clusters (74). Also, as seen with EGFR-mEGFP, the extent of clustering for the EGFR mutants is more pronounced in cholesterol-depleted cells compared with cytoskeleton-disrupted cells. This implies that cholesterol depletion releases the receptors from lipid domains, which allows them to cluster more after EGF stimulation.

The extent of this clustering was different for all the mutants. The triple mutant lacking negative cooperativity (EGFR$^{E685A/E687A/E690A}$-mEGFP) and the GM3-inhibition-insensitive mutant (EGFR^{K642G}-mEGFP) responded similarly to EGFR-mEGFP and showed the formation of large clusters, with the MOM requiring either trimers or tetramers to explain the data (Table S2).

The double mutant with impaired activator and receiver functions (EGFR$^{I706Q/V948R}$-mEGFP) and the multimerization-deficient mutant (EGFR$^{\Delta 550\text{-}580}$-mEGFP) also showed some clustering but to a lesser extent than EGFR-mEGFP, with dimers being sufficient to explain the data (Table S2). In conjunction with the data showing that both these mutants oligomerize less strongly than EGFR-mEGFP (Table 3), this suggests that EGF-induced clustering in actin cytoskeleton-disrupted or cholesterol-depleted cells may not be driven by oligomerization alone but possibly involves grouping of receptors at internalization sites and nonspecific aggregation.

Summary of results

In summary, EGFR oligomerization is influenced by both its structural features and the plasma membrane environment,

and we have quantified the oligomerization using camera-based N&B. In the resting state, EGFR molecules are present as monomers and dimers, and we estimate the dimer fraction to be comprised of ~60% of the receptor population. That said, we cannot exclude the presence of a small amount of higher-order oligomers, as we have shown in a recent study (34). Other previous studies (6,33,74–79) have shown that cholesterol- and sphingolipid-rich lipid domains trap a fraction of the EGFR population and prevent aberrant clustering and activation of the receptor in the resting state. Our quantification shows that disrupting the lipid domains through either cholesterol depletion or sphingolipid removal increases EGFR dimerization. On the other hand, cytoskeletal disruption does not affect EGFR dimerization.

Residues I706 and V948 are located in the activator and receiver lobes in the TKD, respectively, and are required for EGFR phosphorylation (84,88) and linked to EGFR dimerization (33,87). The results here show that they stabilize the dimeric form of the receptor both before and after activation. Mutations to residues E685, E687, and E690 in the JM-A domain show reduced dimerization, corroborating their involvement in negative cooperativity in ligand binding (85). Furthermore, as observed in proteoliposomes earlier, we show in live cells that abolishing GM3 interaction with EGFR through mutation of K642 in the ECD (86) increases receptor dimerization and phosphorylation, suggesting that GM3 acts in an inhibitory fashion to prevent aberrant receptor dimerization and phosphorylation (95–98). Additionally, we also confirm the predictions from simulations that the structural requirements of dimerization differ from those of multimerization and involve different regions of the ECD. For EGFR phosphorylation (and presumably activation), dimerization is insufficient, and oligomerization is necessary.

Finally, we show that EGF stimulation after cholesterol depletion or actin cytoskeleton disruption results in the formation of larger clusters than those achieved by ligand stimulation alone and that this clustering is driven not solely by oligomerization but possibly involves a combination of oligomerization, grouping of receptors in internalization sites, and nonspecific aggregation.

CONCLUSION

The determination of membrane protein oligomerization is an important task in fluorescence microscopy that is complicated by the photophysical properties of fluorophores, resulting in dark states, and the labeling process, which is not complete. The measurement of oligomerization therefore requires careful calibration. Here, we optimized N&B on a TIRFM setup using EMCCD cameras. We determined the probability of fluorescence of some of the most commonly used fluorescent proteins within the system with results that are consistent with confocal N&B measurements (19). Brightness calibration allows us to account for the dark fraction and improve the accuracy of the oligomerization estimates. This calibration procedure is easy to perform, and the determined values here can be directly applied.

Camera-based N&B yields diffraction-limited oligomerization maps of ~1,000 μm^2 obtained in a measurement time of 20 s, and almost real-time analysis (~1 s) using GPU-based parallel processing, suitable for live-cell investigations. We are thus able to quickly visualize and quantify the heterogeneity in EGFR distribution on the cell membrane and any changes upon perturbation unlike many studies, which are limited to studying a single point of interest at a time. Using optimized and calibrated-camera-based N&B to investigate EGFR oligomerization, we determined that it is the result of a complex interplay of intrinsic structural features of the receptor and extrinsic factors including cell membrane organization and composition. We thus provide supporting evidence to those conditions already studied by other groups and add information on the other conditions. Since EGFR is well studied, the fact that we can reproduce the results from other time-consuming studies often performed in vitro with similar results in live cells in a much shorter time demonstrates the validity and utility of the technique for future studies. N&B has future applications in investigating clustering in live cells for other membrane proteins and can be extended to other camera-based imaging modalities, other cameras (34), and other samples.

SUPPORTING MATERIAL

Supporting material can be found online at https://doi.org/10.1016/j.bpj.2022.11.003.

AUTHOR CONTRIBUTIONS

T.W. and H.B. conceived and designed the study. T.W. supervised the study and provided the resources. H.B., S.P., and C.J.H.G. performed the experiments. H.B. and J.S. formulated the N&B equations. H.B and S.P. analyzed the data. H.B., J.S., C.J.H.G., and T.W. wrote the manuscript.

ACKNOWLEDGMENTS

T.W. gratefully acknowledges funding from the Singapore Ministry of Education (MOE2016-T2-2-121). H.B. and S.P. are the recipients of research scholarships of the National University of Singapore. The authors thank Sonia Monti for help with preparing the EGFR figures.

DECLARATION OF INTERESTS

The authors declare no competing interests.

SUPPORTING CITATIONS

References (101–106) appear in the supporting material.

REFERENCES

1. Valley, C. C., K. A. Lidke, and D. S. Lidke. 2014. The spatiotemporal organization of ErbB receptors: insights from microscopy. *Cold Spring Harbor Perspect. Biol.* 6:a020735.
2. Loura, L. M. S., and M. Prieto. 2011. FRET in membrane biophysics: an overview. *Front. Physiol.* 2:82.
3. Asher, W. B., P. Geggier, …, J. A. Javitch. 2021. Single-molecule FRET imaging of GPCR dimers in living cells. *Nat. Methods.* 18:397–405.
4. Macháň, R., and T. Wohland. 2014. Recent applications of fluorescence correlation spectroscopy in live systems. *FEBS Lett.* 588: 3571–3584.
5. Chen, Y., L. N. Wei, and J. D. Müller. 2003. Probing protein oligomerization in living cells with fluorescence fluctuation spectroscopy. *Proc. Natl. Acad. Sci. USA.* 100:15492–15497.
6. Saffarian, S., Y. Li, E. L. Elson, and L. J. Pike. 2007. Oligomerization of the EGF receptor investigated by live cell fluorescence intensity distribution analysis. *Biophys. J.* 93:1021–1031.
7. Swift, J. L., A. G. Godin, …, J. M. Beaulieu. 2011. Quantification of receptor tyrosine kinase transactivation through direct dimerization and surface density measurements in single cells. *Proc. Natl. Acad. Sci. USA.* 108:7016–7021.
8. Godin, A. G., S. Costantino, …, P. W. Wiseman. 2011. Revealing protein oligomerization and densities in situ using spatial intensity distribution analysis. *Proc. Natl. Acad. Sci. USA.* 108:7010–7015.
9. Kolin, D. L., and P. W. Wiseman. 2007. Advances in image correlation spectroscopy: measuring number densities, aggregation states, and dynamics of fluorescently labeled macromolecules in cells. *Cell Biochem. Biophys.* 49:141–164.
10. Dey, S., and S. Maiti. 2018. Single-molecule photobleaching: instrumentation and applications. *J. Biosci.* 43:447–454.
11. Digman, M. A., R. Dalal, …, E. Gratton. 2008. Mapping the number of molecules and brightness in the laser scanning microscope. *Biophys. J.* 94:2320–2332.
12. Dalal, R. B., M. A. Digman, …, E. Gratton. 2008. Determination of particle number and brightness using a laser scanning confocal microscope operating in the analog mode. *Microsc. Res. Tech.* 71:69–81.
13. Qian, H., and E. L. Elson. 1990. Distribution of molecular aggregation by analysis of fluctuation moments. *Proc. Natl. Acad. Sci. USA.* 87:5479–5483.
14. Qian, H., and E. L. Elson. 1990. On the analysis of high order moments of fluorescence fluctuations. *Biophys. J.* 57:375–380.
15. Unruh, J. R., and E. Gratton. 2008. Analysis of molecular concentration and brightness from fluorescence fluctuation data with an electron multiplied CCD camera. *Biophys. J.* 95:5385–5398.
16. Nolan, R., M. Iliopoulou, …, S. Padilla-Parra. 2018. Detecting protein aggregation and interaction in live cells: a guide to number and brightness. *Methods.* 140–141:172–177.
17. Foo, Y. H., N. Naredi-Rainer, …, T. Wohland. 2012. Factors affecting the quantification of biomolecular interactions by fluorescence cross-correlation spectroscopy. *Biophys. J.* 102:1174–1183.
18. Cranfill, P. J., B. R. Sell, …, D. W. Piston. 2016. Quantitative assessment of fluorescent proteins. *Nat. Methods.* 13:557–562.
19. Dunsing, V., M. Luckner, …, S. Chiantia. 2018. Optimal fluorescent protein tags for quantifying protein oligomerization in living cells. *Sci. Rep.* 8:10634.
20. Chen, Y., J. Johnson, …, J. D. Mueller. 2010. Observing Protein Interactions and Their Stoichiometry in Living Cells by Brightness Analysis of Fluorescence Fluctuation Experiments, 1st ed. Elsevier Inc.
21. Vámosi, G., N. Mücke, …, K. Tóth. 2016. EGFP oligomers as natural fluorescence and hydrodynamic standards. *Sci. Rep.* 6:1–12.
22. Rodriguez, E. A., R. E. Campbell, …, R. Y. Tsien. 2017. The growing and glowing toolbox of fluorescent and photoactive proteins. *Trends Biochem. Sci.* 42:111–129.
23. Lemmon, M. A., and J. Schlessinger. 2010. Cell signaling by receptor tyrosine kinases. *Cell.* 141:1117–1134.
24. Moriki, T., H. Maruyama, and I. N. Maruyama. 2001. Activation of preformed EGF receptor dimers by ligand-induced rotation of the transmembrane domain. *J. Mol. Biol.* 311:1011–1026.
25. Ziomkiewicz, I., A. Loman, …, D. J. Arndt-Jovin. 2013. Dynamic conformational transitions of the EGF receptor in living mammalian cells determined by FRET and fluorescence lifetime imaging microscopy. *Cytometry A.* 83:794–805.
26. Wang, Y., J. Gao, …, H. Wang. 2014. Regulation of EGFR nanocluster formation by ionic protein-lipid interaction. *Cell Res.* 24:959–976.
27. Kluba, M., Y. Engelborghs, …, H. Mizuno. 2015. Inhibition of receptor dimerization as a novel negative feedback mechanism of EGFR signaling. *PLoS One.* 10:e0139971.
28. Yamashita, H., Y. Yano, …, K. Matsuzaki. 2015. Oligomerization-function relationship of EGFR on living cells detected by the coiled-coil labeling and FRET microscopy. *Biochim. Biophys. Acta.* 1848:1359–1366.
29. Byrne, P. O., K. Hristova, and D. J. Leahy. 2020. EGFR forms ligand-independent oligomers that are distinct from the active state. *J. Biol. Chem.* 295:13353–13362.
30. Tao, R. H., and I. N. Maruyama. 2008. All EGF(ErbB) receptors have preformed homo- and heterodimeric structures in living cells. *J. Cell Sci.* 121:3207–3217.
31. Liu, P., T. Sudhaharan, …, T. Wohland. 2007. Investigation of the dimerization of proteins from the epidermal growth factor receptor family by single wavelength fluorescence cross-correlation spectroscopy. *Biophys. J.* 93:684–698.
32. Ma, X., S. Ahmed, and T. Wohland. 2011. EGFR activation monitored by SW-FCCS in live cells. *Front. Biosci.* 3:22–32.
33. Yavas, S., R. Macháň, and T. Wohland. 2016. The epidermal growth factor receptor forms location-dependent complexes in resting cells. *Biophys. J.* 111:2241–2254.
34. Sankaran, J., H. Balasubramanian, …, T. Wohland. 2021. Simultaneous spatiotemporal super-resolution and multi-parametric fluorescence microscopy. *Nat. Commun.* 12:1748.
35. Zanetti-Domingues, L. C., D. Korovesis, …, M. L. Martin-Fernandez. 2018. The architecture of EGFR's basal complexes reveals autoinhibition mechanisms in dimers and oligomers. *Nat. Commun.* 9:4325.
36. Nagy, P., J. Claus, …, D. J. Arndt-Jovin. 2010. Distribution of resting and ligand-bound ErbB1 and ErbB2 receptor tyrosine kinases in living cells using number and brightness analysis. *Proc. Natl. Acad. Sci. USA.* 107:16524–16529.
37. Low-Nam, S. T., K. A. Lidke, …, D. S. Lidke. 2011. ErbB1 dimerization is promoted by domain co-confinement and stabilized by ligand binding. *Nat. Struct. Mol. Biol.* 18:1244–1249.
38. Kovacs, E., J. A. Zorn, …, J. Kuriyan. 2015. A structural perspective on the regulation of the epidermal growth factor receptor. *Annu. Rev. Biochem.* 84:739–764.
39. Freed, D. M., N. J. Bessman, …, M. A. Lemmon. 2017. EGFR ligands differentially stabilize receptor dimers to specify signaling kinetics. *Cell.* 171:683–695.e18.
40. Thirukkumaran, O. M., M. Kluba, …, H. Mizuno. 2020. Autophosphorylation of EGFR at Y954 facilitated homodimerization and enhanced downstream signals. *Biophys. J.* 119:2127–2137.
41. Clayton, A. H. A., F. Walker, …, A. W. Burgess. 2005. Ligand-induced dimer-tetramer transition during the activation of the cell surface epidermal growth factor receptor-A multidimensional microscopy analysis. *J. Biol. Chem.* 280:30392–30399.
42. Clayton, A. H. A., S. G. Orchard, …, A. W. Burgess. 2008. Predominance of activated EGFR higher-order oligomers on the cell surface. *Growth Factors.* 26:316–324.
43. Kozer, N., D. Barua, …, A. H. A. Clayton. 2013. Exploring higher-order EGFR oligomerisation and phosphorylation - a combined experimental and theoretical approach. *Mol. Biosyst.* 9:1849–1863.

44. Kozer, N., D. Barua, …, A. H. A. Clayton. 2014. Recruitment of the adaptor protein Grb2 to EGFR tetramers. *Biochemistry.* 53: 2594–2604.

45. Needham, S. R., S. K. Roberts, …, M. L. Martin-Fernandez. 2016. EGFR oligomerization organizes kinase-active dimers into competent signalling platforms. *Nat. Commun.* 7:13307–13314.

46. Needham, S. R., L. C. Zanetti-Domingues, …, D. T. Clarke. 2014. Structure-function relationships and supramolecular organization of the EGFR (epidermal growth factor receptor) on the cell surface. *Biochem. Soc. Trans.* 42:114–119.

47. Sankaran, J., H. Balasubramanian, …, T. Wohland. 2021. Preparation of live cell samples for fluorescence spectroscopy and computational super-resolution imaging. *Protoc. Exch.*

48. Sankaran, J., H. Balasubramanian, …, T. Wohland. 2021. Simultaneous spatiotemporal computational super-resolution and multi-parametric fluorescence microscopy. *Protoc. Exch.*

49. Sankaran, J., H. Balasubramanian, …, T. Wohland. 2021. Imaging FCS 1.52. https://github.com/ImagingFCS/Imaging_FCS_1_52.

50. Sankaran, J., N. Bag, R. S. Kraut, and T. Wohland. 2013. Accuracy and precision in camera-based fluorescence correlation spectroscopy measurements. *Anal. Chem.* 85:3948–3954.

51. Ries, J., S. Chiantia, and P. Schwille. 2009. Accurate determination of membrane dynamics with line-scan FCS. *Biophys. J.* 96:1999–2008.

52. Wohland, T., S. Maiti, and R. Macháň. 2020. An Introduction to Fluorescence Correlation Spectroscopy. IOP Publishing.

53. Krieger, J. W., A. P. Singh, …, T. Wohland. 2015. Imaging fluorescence (cross-) correlation spectroscopy in live cells and organisms. *Nat. Protoc.* 10:1948–1974.

54. Trullo, A., V. Corti, …, M. Zamai. 2013. Application limits and data correction in number of molecules and brightness analysis. *Microsc. Res. Tech.* 76:1135–1146.

55. Meiresonne, N. Y., E. Consoli, …, T. den Blaauwen. 2019. Superfolder mTurquoise2 ox optimized for the bacterial periplasm allows high efficiency in vivo FRET of cell division antibiotic targets. *Mol. Microbiol.* 111:1025–1038.

56. Shaner, N. C., G. G. Lambert, …, J. Wang. 2013. A bright monomeric green fluorescent protein derived from Branchiostoma lanceolatum. *Nat. Methods.* 10:407–409.

57. Paez-Segala, M. G., M. G. Sun, …, L. L. Looger. 2015. Fixation-resistant photoactivatable fluorescent proteins for CLEM. *Nat. Methods.* 12:215–218.

58. Bajar, B. T., A. J. Lam, …, M. Z. Lin. 2016. Fluorescent indicators for simultaneous reporting of all four cell cycle phases. *Nat. Methods.* 13:993–996.

59. Bindels, D. S., L. Haarbosch, …, T. W. J. Gadella. 2017. mScarlet: a bright monomeric red fluorescent protein for cellular imaging. *Nat. Methods.* 14:53–56.

60. Costantini, L. M., M. Baloban, …, E. L. Snapp. 2015. A palette of fluorescent proteins optimized for diverse cellular environments. *Nat. Commun.* 6:7670.

61. Manna, P., S. T. Hung, …, R. Jimenez. 2018. Directed evolution of excited state lifetime and brightness in FusionRed using a microfluidic sorter. *Integr. Biol.* 10:516–526.

62. Goedhart, J., D. Von Stetten, …, A. Royant. 2012. Structure-guided evolution of cyan fluorescent proteins towards a quantum yield of 93. *Nat. Commun.* 3:751.

63. Zacharias, D. A., J. D. Violin, …, R. Y. Tsien. 2002. Partitioning of lipid-modified monomeric GFPs into membrane microdomains of live cells. *Science.* 296:913–916.

64. Shaner, N. C., M. Z. Lin, …, R. Y. Tsien. 2008. Improving the photostability of bright monomeric orange and red fluorescent proteins. *Nat. Methods.* 5:545–551.

65. Shaner, N. C., R. E. Campbell, …, R. Y. Tsien. 2004. Improved monomeric red, orange and yellow fluorescent proteins derived from Discosoma sp. red fluorescent protein. *Nat. Biotechnol.* 22:1567–1572.

66. Shen, Y., Y. Chen, …, R. E. Campbell. 2017. Engineering of mCherry variants with long Stokes shift, red-shifted fluorescence, and low cytotoxicity. *PLoS One.* 12:e0171257.

67. Shcherbo, D., C. S. Murphy, …, D. M. Chudakov. 2009. Far-red fluorescent tags for protein imaging in living tissues. *Biochem. J.* 418:567–574.

68. Liu, P. 2007. The Study of Interactions of Transmembrane Receptors and Intracellular Signaling Proteins in Live Cells by Fluorescence Correlation and Cross-Correlation Spectroscopy. National University, PhD thesis.

69. Vasilyev, F. F., J. A. Lopatnikova, and S. V. Sennikov. 2013. Optimized flow cytometry protocol for analysis of surface expression of interleukin-1 receptor types I and II. *Cytotechnology.* 65:795–802.

70. Chiu, C.-S., E. Kartalov, …, H. A. Lester. 2001. Single-molecule measurements calibrate green fluorescent protein surface densities on transparent beads for use with 'knock-in' animals and other expression systems. *J. Neurosci. Methods.* 105:55–63.

71. Lidke, D. S., P. Nagy, …, T. M. Jovin. 2004. Quantum dot ligands provide new insights into erbB/HER receptor-mediated signal transduction. *Nat. Biotechnol.* 22:198–203.

72. Kozer, N., and A. H. A. Clayton. 2020. In-cell structural dynamics of an EGF receptor during ligand-induced dimer–oligomer transition. *Eur. Biophys. J.* 49:21–37.

73. Ariotti, N., H. Liang, …, S. J. Plowman. 2010. Epidermal growth factor receptor activation remodels the plasma membrane lipid environment to induce nanocluster formation. *Mol. Cell Biol.* 30:3795–3804.

74. Bag, N., S. Huang, and T. Wohland. 2015. Plasma membrane organization of epidermal growth factor receptor in resting and ligand-bound states. *Biophys. J.* 109:1925–1936.

75. Ringerike, T., F. D. Blystad, …, E. Stang. 2002. Cholesterol is important in control of EGF receptor kinase activity but EGF receptors are not concentrated in caveolae. *J. Cell Sci.* 115:1331–1340.

76. Chen, X., and M. D. Resh. 2002. Cholesterol depletion from the plasma membrane triggers ligand-independent activation of the epidermal growth factor receptor. *J. Biol. Chem.* 277:49631–49637.

77. Webb, S. E. D., M. Hirsch, …, D. J. Rolfe. 2015. Nanometric molecular separation measurements by single molecule photobleaching. *Methods.* 88:76–80.

78. Pike, L. J., and L. Casey. 2002. Cholesterol levels modulate EGF receptor-mediated signaling by altering receptor function and trafficking. *Biochemistry.* 41:10315–10322.

79. Pike, L. J. 2005. Growth factor receptors, lipid rafts and caveolae: an evolving story. *Biochim. Biophys. Acta.* 1746:260–273.

80. Gupta, A., D. Lu, …, T. Wohland. 2022. Heptanol-mediated phase separation determines phase preference of molecules in live cell membranes. *J. Lipid Res.* 63:100220.

81. Sezgin, E., I. Levental, …, C. Eggeling. 2017. The mystery of membrane organization: composition, regulation and roles of lipid rafts. *Nat. Rev. Mol. Cell Biol.* 18:361–374.

82. Miyake, Y., Y. Kozutsumi, …, T. Kawasaki. 1995. Serine palmitoyltransferase is the primary target of a sphingosine-like immunosuppressant, ISP-1/myriocin. *Biochem. Biophys. Res. Commun.* 211: 396–403.

83. Davis, R. J., N. Gironès, and M. Faucher. 1988. Two alternative mechanisms control the interconversion of functional states of the epidermal growth factor receptor. *J. Biol. Chem.* 263:5373–5379.

84. Kiuchi, T., E. Ortiz-Zapater, …, T. Ng. 2014. The ErbB4 CYT2 variant protects EGFR from ligand-induced degradation to enhance cancer cell motility. *Sci. Signal.* 7:ra78.

85. Adak, S., K. S. Yang, …, L. J. Pike. 2011. The membrane-proximal intracellular domain of the epidermal growth factor receptor underlies negative cooperativity in ligand binding. *J. Biol. Chem.* 286:45146–45155.

86. Coskun, Ü., M. Grzybek, …, K. Simons. 2011. Regulation of human EGF receptor by lipids. *Proc. Natl. Acad. Sci. USA.* 108:9044–9048.

87. Huang, Y., S. Bharill, …, J. Kuriyan. 2016. Molecular basis for multimerization in the activation of the epidermal growth factor receptor. *Elife.* 5:e14107–e14127.

88. Zhang, X., J. Gureasko, …, J. Kuriyan. 2006. An allosteric mechanism for activation of the kinase domain of epidermal growth factor receptor. *Cell.* 125:1137–1149.

89. Adak, S., D. DeAndrade, and L. J. Pike. 2011. The tethering arm of the EGF receptor is required for negative cooperativity and signal transduction. *J. Biol. Chem.* 286:1545–1555.

90. Macdonald-Obermann, J. L., and L. J. Pike. 2009. The intracellular juxtamembrane domain of the epidermal growth factor (EGF) receptor is responsible for the allosteric regulation of EGF binding. *J. Biol. Chem.* 284:13570–13576.

91. Li, Y., J. Macdonald-Obermann, …, L. J. Pike. 2012. Quantitation of the effect of ErbB2 on epidermal growth factor receptor binding and dimerization. *J. Biol. Chem.* 287:31116–31125.

92. Macdonald-Obermann, J. L., and L. J. Pike. 2018. Allosteric regulation of epidermal growth factor (EGF) receptor ligand binding by tyrosine kinase inhibitors. *J. Biol. Chem.* 293:13401–13414.

93. Abd Halim, K. B., H. Koldsø, and M. S. P. Sansom. 2015. Interactions of the EGFR juxtamembrane domain with PIP2-containing lipid bilayers: insights from multiscale molecular dynamics simulations. *Biochim. Biophys. Acta.* 1850:1017–1025.

94. Maeda, R., T. Sato, …, Y. Sako. 2018. Lipid-protein interplay in dimerization of juxtamembrane domains of epidermal growth factor receptor. *Biophys. J.* 114:893–903.

95. Yoon, S. J., K. I. Nakayama, …, S. I. Hakomori. 2006. Epidermal growth factor receptor tyrosine kinase is modulated by GM3 interaction with N-linked GlcNAc termini of the receptor. *Proc. Natl. Acad. Sci. USA.* 103:18987–18991.

96. Nakano, M., S. Hanashima, …, M. Murata. 2021. FRET detects lateral interaction between transmembrane domain of EGF receptor and ganglioside GM3 in lipid bilayers. *Biochim. Biophys. Acta Biomembr.* 1863:183623.

97. Hedger, G., D. Shorthouse, …, M. S. P. Sansom. 2016. Free energy landscape of lipid interactions with regulatory binding sites on the transmembrane domain of the EGF receptor. *J. Phys. Chem. B.* 120:8154–8163.

98. Kim, C. 2020. GM3 Signaling. Springer Singapore.

99. Gupta, A., S. Muralidharan, …, T. Wohland. 2020. Long acyl chain ceramides govern cholesterol and cytoskeleton dependence of membrane outer leaflet dynamics. *Biochim. Biophys. Acta Biomembr.* 1862, 183153.

100. Komura, N., K. G. N. Suzuki, …, M. Kiso. 2016. Raft-based interactions of gangliosides with a GPI-anchored receptor. *Nat. Chem. Biol.* 12:402–410.

101. Chapple, J. P., A. J. Hardcastle, …, M. E. Cheetham. 2000. Mutations in the N-terminus of the X-linked retinitis pigmentosa protein RP2 interfere with the normal targeting of the protein to the plasma membrane. *Hum. Mol. Genet.* 9:1919–1926.

102. Chapple, J. P., A. J. Hardcastle, …, M. E. Cheetham. 2002. Delineation of the plasma membrane targeting domain of the X-linked retinitis pigmentosa protein RP2. *Invest. Ophthalmol. Vis. Sci.* 43:2015–2020.

103. Fowler, D. K., S. Stewart, …, P. Washbourne. 2016. A MultiSite Gateway toolkit for rapid cloning of vertebrate expression constructs with diverse research applications. *PLoS One.* 11:e0159277.

104. Kozer, N., M. P. Kelly, …, A. H. A. Clayton. 2011. Differential and synergistic effects of epidermal growth factor receptor antibodies on unliganded ErbB dimers and oligomers. *Biochemistry.* 50:3581–3590.

105. Bader, A. N., E. G. Hofman, …, H. C. Gerritsen. 2009. Homo-FRET imaging enables quantification of protein cluster sizes with subcellular resolution. *Biophys. J.* 97:2613–2622.

106. Hofman, E. G., A. N. Bader, …, P. M. P. Van Bergen en Henegouwen. 2010. Ligand-induced EGF receptor oligomerization is kinase-dependent and enhances internalization. *J. Biol. Chem.* 285:39481–39489.